Volume 14
Number 29
7 August 2022
Pages 10257-10596

Nanoscale

rsc.li/nanoscale

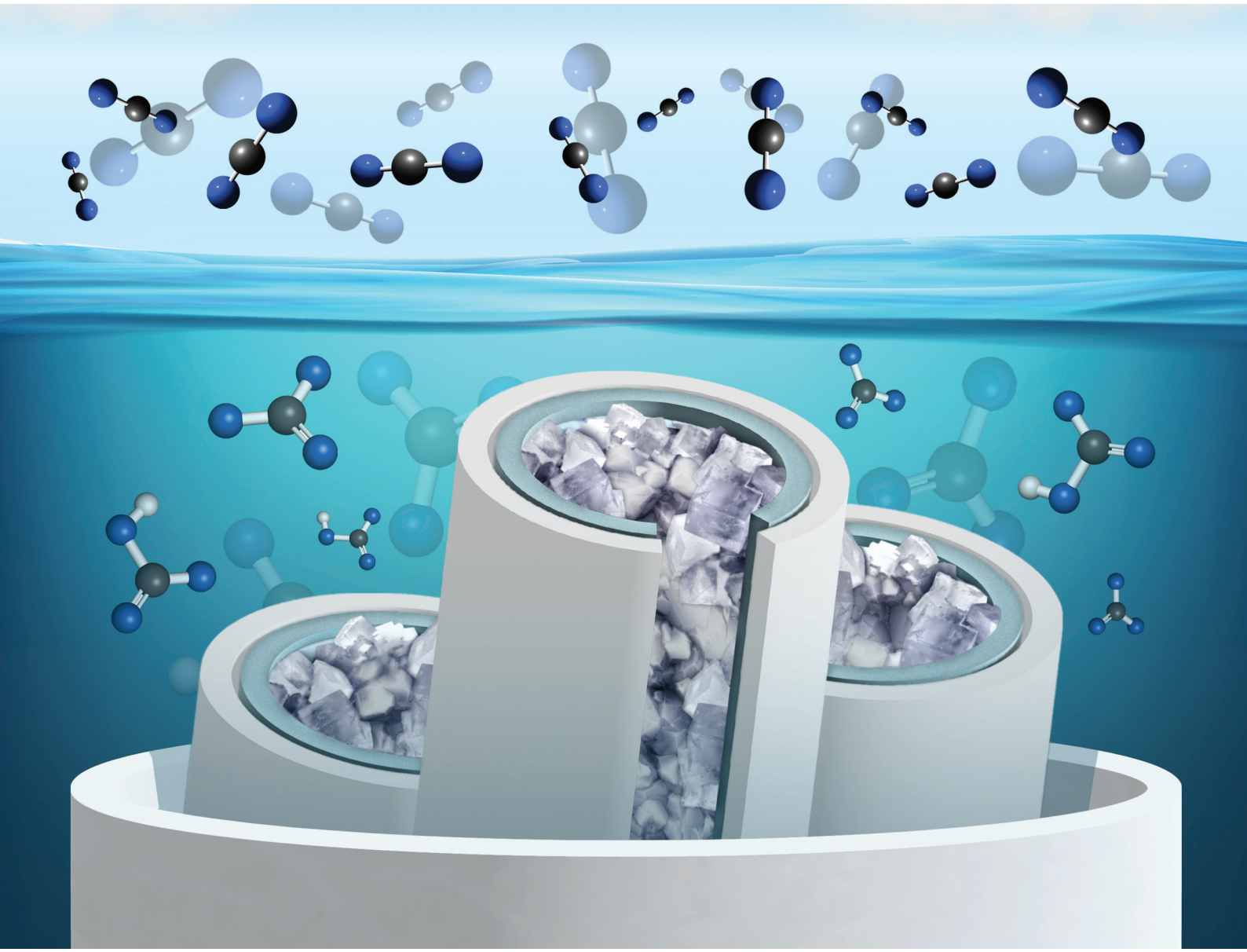

ISSN 2040-3372

ROYAL SOCIETY OF CHEMISTRY

PAPER
Greeshma Gadikota *et al.*
Confinement induces stable calcium carbonate formation in silica nanopores

NCNST

Nanoscale

PAPER

View Article Online
View Journal | View Issue

Cite this: *Nanoscale*, 2022, **14**, 10349

Confinement induces stable calcium carbonate formation in silica nanopores†

Hassnain Asgar,‡ Sohaib Mohammed ‡ and Greeshma Gadikota *

Received 2nd April 2022,
Accepted 17th June 2022

DOI: 10.1039/d2nr01834a

rsc.li/nanoscale

Scalable efforts to remove anthropogenic CO_2 *via* the formation of durable carbonates require us to harness siliceous nanoporous geologic materials for carbon storage. While calcium carbonate formation has been extensively reported in bulk fluids, there is a limited understanding of the influence of nano-confined fluids on the formation of specific stable and metastable polymorphs of calcium carbonates in siliceous materials that are abundant in subsurface environments. To address this challenge, silica nanochannels with diameters of 3.7 nm are architected and the formation of specific calcium carbonate phases is investigated using X-ray diffraction (XRD), and molecular dynamics (MD) simulations. The formation of stable calcium carbonate (or calcite) is noted in silica nanochannels. The presence of fewer water molecules in the first hydration shell of calcium ions in confinement compared to in bulk fluids contributes to stable calcium carbonate formation. These studies show that nanoporous siliceous environments favor the formation of stable calcium carbonate formation.

1. Introduction

Carbonate transformations regulate carbon cycling and maintain the earth's ecological balance. Rising anthropogenic CO_2 concentrations in the air contribute to increasing global temperatures[1] due to the greenhouse effect[2] and threaten our ecological balance.[3] Achieving tunable controls on carbon transformations is crucial for developing engineered processes for decarbonization and achieving net negative carbon emission goals.[4,5] Several approaches have been proposed to capture and convert anthropogenic CO_2 emissions.[6,7] Among these approaches, carbon mineralization which involves converting CO_2 into solid inorganic carbonates[8] is thermodynamically downhill and can be engineered to store several gigatons of CO_2.[9,10] Carbon mineralization can be realized through the direct chemical interactions of solid calcium and magnesium-bearing alkaline solid or aqueous resources with gaseous CO_2 or by dissolving CO_2 in water to produce (bi)carbonate-rich fluids that react to produce solid calcium and magnesium carbonates.[11,12] The accelerated conversion of mobile CO_2 into solid carbonates in subsurface geologic environments ensures permanent and safe storage and limits the need to monitor the fate of CO_2 over several years. Similarly, engineered removal of CO_2 from air and water to produce solid carbonates is a durable and quantifiable carbon management approach.

Despite the gigaton-scale potential for storing CO_2 in reactive subsurface formations such as basalt[13] and olivine,[14] estimating the time scales of carbon mineralization is a challenge due to anomalous carbon mineralization behavior in nanoconfinement.[15,16] Pore sizes in ultramafic minerals and rocks such as olivine and basalt can be smaller than 20 nm.[17] In these nanoporous environments, the interfacial organization of pore fluids contributes to anomalous carbonate crystallization behavior that differs significantly from that of bulk fluids.

Achieving predictive control over the formation of calcium or magnesium carbonates in confinement is crucial for several reasons. First, this approach enables the reconciliation of faster than expected carbon mineralization rates in subsurface environments as opposed to predicted rates as noted in the CarbFix project.[13] Second, resolving the influence of interfacial water on the formation of metastable or stable carbonate phases is crucial for developing engineered strategies for carbon removal using porous materials. Third, the role of confinement in directing the formation of specific carbonate phases preferentially assists with determining the associated impact on storing gigaton levels of CO_2 in these environments. The formation of stable carbonates such as calcite ($CaCO_3$) or magnesite ($MgCO_3$) is preferred since the structures of stable carbonate remain unchanged over a long period and stoichiometric utilization of Ca^{2+} or Mg^{2+} ions to produce stable carbonates is achieved. Stable carbonate phases have lower solubility compared to metastable phases.[18,19] Metastable carbon-

School of Civil and Environmental Engineering, Cornell University, Ithaca, NY 14853, USA. E-mail: gg464@cornell.edu; Tel: +1 607-255-4796

†Electronic supplementary information (ESI) available. See DOI: https://doi.org/10.1039/d2nr01834a

‡Equal contribution.

ates, in contrast, gradually transform into stable carbonates over time.[20] Examples of metastable calcium carbonate phases include spherical vaterite ($CaCO_3$) and rosette-shaped aragonite ($CaCO_3$).[21,22] Examples of metastable magnesium carbonates include needle-like nesquehonite ($MgCO_3{\cdot}3H_2O$),[23] sheet-like hydromagnesite ($(MgCO_3)_3(Mg(OH)_2)_2{\cdot}4H_2O$),[24] and platy lansfordite ($MgCO_3{\cdot}5H_2O$).[23] The formation of magnesium hydroxide in hydromagnesite is a less effective use of magnesium as opposed to the complete utilization of magnesium to produce magnesite.

The confinement-mediated behavior of carbonates formation has been studied in the context of biomineralization[20,25–27] to understand exoskeleton growth in invertebrates. However, a mechanistic understanding of how carbonates form in subsurface abundant nano-porous (pore sizes 2–50 nm) siliceous matter remains unresolved despite the rising interest in engineered carbon transformations for a sustainable climate, energy, and environmental future. While prior studies reported the formation and stabilization of amorphous calcium carbonate in micron-level confinement,[28] the influence of nanoscale confinement on the preferential formation of stable or metastable calcium carbonate phases has not been studied. Various carbonate crystallization mechanisms have been proposed to describe nucleation and growth mechanisms in bulk fluids but are applicable under limited conditions. Classical nucleation growth (CNG), which describes a first-order transition occurring *via* (i) nucleation of a solid phase and (ii) subsequent spontaneous growth,[29] and classical crystal growth theory (CGT), which suggests a layer-by-layer growth of carbonates once a critical size is reached, are applicable in limited scenarios.[30,31] Alternatively, the Ostwald rule of stages, in which the formation of stable crystalline phases is mediated by intermediate metastable carbonate states with lower free energy barriers to nucleation, explains specific observations related to stable calcite formation.[32] However, this theory does not explain observations of the direct formation of stable carbonates.[33]

For crystal sizes smaller than 100 nm, size-dependent variation in the enthalpic contributions of the free energy and small variations in enthalpic differences (*e.g.*, 1–10 kJ mol^{-1}) was proposed to explain the formation of metastable vaterite, aragonite, and then calcite.[34] It is hypothesized that metastable to stable carbonate changes occur *via* solid-state transformations and dissolution–reprecipitation mechanisms. For example, the transformations of amorphous calcium carbonate (ACC) to biominerals that occur in the absence of water are attributed to solid-state transformations.[35] Alternatively, the dissolution of more soluble metastable phases to produce more stable and less soluble phases has been proposed.[36] This phenomenon, which is based on the differences in the solubility of phases, is analogous to "Ostwald ripening", which describes size-dependent dissolution and reprecipitation behavior.

Other non-classical theories such as "oriented attachment" describe the spontaneous self-assembly of nanocrystalline particles along crystallographic faces to aid particle-mediated growth of 1D, 2D, and 3D crystals.[26,37,38] It was also hypothesized that differences in the ordering of the solvent at solid interfaces and around ions can create free energy minima where nanoparticles can reside without aggregating before the formation of a meso-crystalline structure.[39] Despite these mechanistic insights, the dual effects of surface interactions and nanoscale confinement on carbonate formation in siliceous nanopores with sizes ranging from 2 nm to 50 nm remain unresolved. Advancing predictive controls into the carbon mineralization behavior in silica nanopores is crucial for estimating the time scales for converting mobile CO_2 into stable carbonates. Conversion of mobile CO_2 into mineralized solids limits the need to track the fate of fluidic CO_2 and eliminates the risk of CO_2 ex-solution and preferential partitioning into the atmosphere.

In carbon mineralization for Ca- and Mg-silicate interfaces, the reactions proceed in two steps: (i) release of Ca^{2+} or Mg^{2+} ions by the dissolution of silicate phases in acidic conditions, and (ii) nucleation of solid carbonates at pH > 8.[40] Carbon mineralization occurs when the concentrations of the dissolved cations and carbonate species reaches supersaturation. Limiting conditions for carbon mineralization can include CO_2 solvation, the insufficient concentration of dissolved Ca and Mg species, and solid carbonate precipitation. Prior work in bulk fluids has shown that dissolved carbonate concentrations from anthropogenic CO_2 can be enhanced using biomimetic catalysts such as carbonic anhydrase[41,42] and solvents such as amines and amino acids.[43–45] Sufficiently high concentrations of dissolved carbonate ions in fluids bearing calcium ions favor calcium carbonate precipitation. In this work, the influence of nanoscale confinement and silica interfaces on directing the formation of stable or metastable calcium carbonate phases is investigated. The specific scientific questions that motivate this study are: (a) How do we architect silica nanochannels with ordered geometry and porosity to investigate the influence of confinement on carbon mineralization? (b) What are the preferred structural orientations of calcium carbonate grown in nanoscale confined environments? (c) What is the influence of the organization of ions in confinement and surface interactions on calcium carbonate formation in nanoscale confinement?

To address these research questions, silica nanochannels with well-ordered vertically aligned pores with sizes of 3.7 nm are synthesized within alumina membranes using a sol–gel approach. Calcium carbonate formation in these nanopores is achieved by reacting solutions of 0.1 M calcium nitrate ($Ca(NO_3)_2$) and 0.1 M sodium bicarbonate ($NaHCO_3$). The influence of the differences in the hydration structure of Ca^{2+} ions at the pore surface and in the center of the pore on the formation of calcium carbonate phases are inferred from molecular dynamics (MD) simulations. This approach of developing architected materials to investigate calcium carbonate formation in a calibrated manner sheds insights into the role of silica interfaces, interfacial fluids, and hydration structure of Ca^{2+} ions in confinement on the preferential formation of specific calcium carbonate phases in confinement. Fig. 1 is a

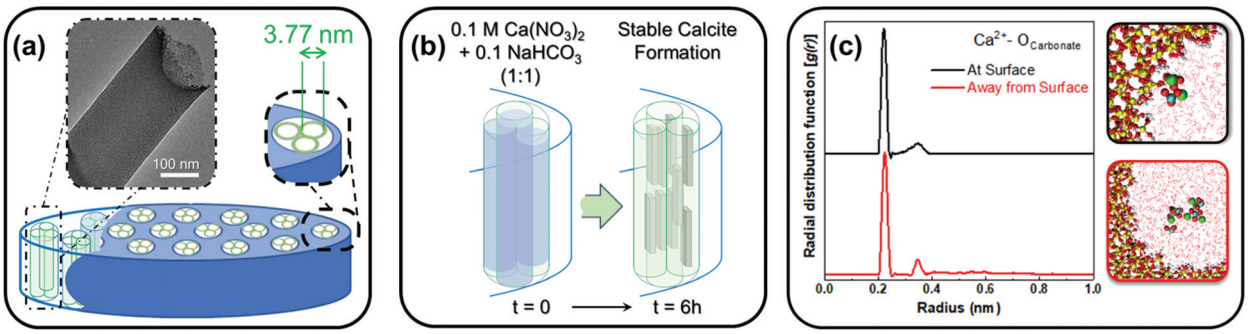

Fig. 1 Schematic representation for (a) synthesis of silica nanochannels in alumina membranes, and (b) the formation of solid carbonates in silica nanochannels. (c) Radial distribution functions (RDFs) for Ca^{2+}–$O_{carbonate}$ species 'at the pore surface' and 'pore center' obtained from molecular dynamics simulations, and the corresponding snapshots of the simulations.

schematic representation of the research approach. These study is particularly relevant since silica-based minerals and rocks are abundant in subsurface environments[10,13] where CO_2 storage *via* carbon mineralization at the scale of several gigatons is proposed.

2. Materials and methods

2.1 Synthesis of silica nanochannels

Silica nanochannels (SNCs) with well-defined pore sizes within anodic alumina membranes (AAMs) are synthesized using a sol–gel approach. AAMs (Cytiva Whatman™ Anodisc™) having a diameter of 25 mm and a thickness of 60 μm are used. Silica is hydrolyzed from tetraethylorthosilicate (TEOS) in ethanol and hydrochloric acid (HCl), while cetyltrimethylammonium bromide (CTAB) is used as the structure-directing agent. In a typical synthesis method, 7.68 g of ethanol, 11.57 g of TEOS, and 1 mL of 2.8 mM HCl are mixed at 60 °C for 90 minutes under reflux to pre-hydrolyze the solution. In a separate beaker, 1.52 g of CTAB is dissolved in 4 mL of 55 mM HCl, and 15 g of ethanol under stirring for 30 minutes at 200 rpm using the magnetic stirrer. Both solutions are mixed for 15 minutes at 400 rpm. To synthesize SNCs in AAMs (pore sizes in AAM ~200 nm, pore length ~60 μm), the empty membranes are loaded on the aspiration setup (Fig. 2), and 0.5 mL of mixture solution is added to the membrane under applied aspiration. Once the solution is passed through the membrane, 0.5 mL is added again and allowed to pass through the membrane. This step is repeated 5 times and the membranes are removed from the setup and rinsed with ethanol to avoid any precipitation on the sides of the membranes. Finally, the membranes are placed at room temperature and the reaction is allowed to proceed for 24 hours, which governs the formation of SNCs inside the pores of AAMs. CTAB is removed from the inside of SNCs by heating AAM-SNCs at 250 °C for 4 hours in a bench-top muffle furnace (Thermo Scientific Thermolyne FB1410 M, Asheville, NC). The temperature corresponding to the decomposition of CTAB is estimated from the thermo-gravimetric analysis of AAM-SNCs, where the major weight loss associated with the degradation of CTAB is noted ~250 °C (Fig. S1(a)†).

The weight (%) changes in the samples of interest during thermal treatment are determined up to 800 °C with a ramp rate of 5 °C min^{-1} in an N_2 environment (purged at 25 mL min^{-1}) using a Thermogravimetric Analyzer (TGA) (TA

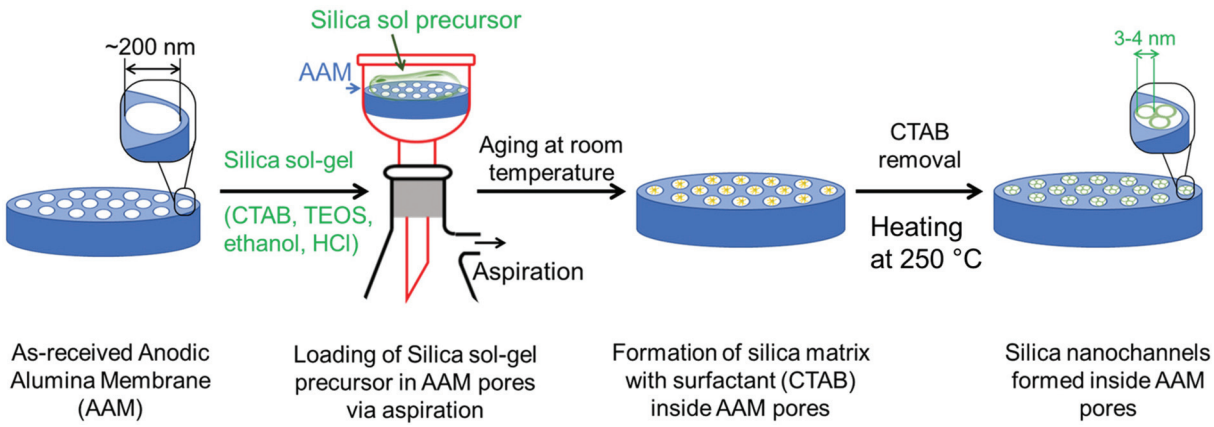

Fig. 2 Schematic representation of steps involved in the synthesis of silica nanochannels (SNCs) inside the alumina membrane.

Instruments, SDT650, New Castle, DE). The pore size distribution and specific surface area of silica nanochannels in AAM (AAM-SNCs) are determined using the nonlocal density functional theory (NLDFT, Quantochrome AutoSorb iQ Analyzer, Boynton Beach, FL) using N_2 adsorption isotherm at 77 K. Before measuring the isotherms, the sample is outgassed at 90 °C for 24 hours. The morphological changes during the synthesis of silica nanochannels are imaged using a scanning electron microscope (Zeiss LEO 1550 FESEM) and transmission electron microscope (FEI F20 TEM) at 200 kV.

2.2 Formation of calcium carbonate in confinement

To investigate the formation of calcium carbonate ($CaCO_3$) phases in confinement, 0.1 M $Ca(NO_3)_2$ and 0.1 M $NaHCO_3$ solutions are mixed in a molar ratio of 1 : 1 and added to silica nanochannels (SNCs) constructed in anodic alumina membranes. A solution comprising 0.1 M $Ca(NO_3)_2$ and 0.1 M $NaHCO_3$ was loaded into the silica nanochannels using an aspiration setup (Fig. S2†). The loading of the solutions into the silica nanochannels is repeated five times to ensure full penetration into SNCs. The outer surfaces of the membranes are cleaned with DI water to prevent calcium carbonate formation outside the silica nanochannels. The structural evolution of the calcium carbonate phases is determined using an X-ray diffractometer (XRD) (Bruker D8 Advance ECO Powder Diffractometer) with Cu Kα radiation, the acceleration voltage of 40 kV, and current of 25 mA. The XRD patterns are obtained in the range of 2θ = 20°–80° after 6, 18, and 30 hours of reaction time.

2.3 Investigation of ion hydration and transport behavior using MD simulations

The hypothesis that the anomalous formation of calcium carbonate phases in confinement compared to bulk fluids emerges from interactions with the silica surfaces, hydration structure of calcium ions, and organization of interfacial fluids is investigated using molecular dynamics simulations. For comparison, simulations of dissolved calcium ions in bulk fluids are performed. Briefly, 0.1 M $CaCO_3$ solutions are simulated as bulk fluids while confined in cylindrical silica nanopores with pore diameters of 3.7 nm at 298 K and 1 bar. The simulation cell for investigating the hydration structure of calcium ions in bulk fluids has dimensions of 6 nm × 6 nm × 6 nm in x, y, and z directions, respectively. The confinement environment is composed of a cylindrical silica pore with 1 g cm^{-3} of 0.1 M $CaCO_3$ solution. The pore (dia. 3.7 nm) is cleaved in an amorphous silica matrix with dimensions of 10.69 nm × 6.42 nm × 6.42 nm in x, y, and z directions, respectively. The simulation cells used for investigating the hydration structure of calcium ions in bulk and confined configurations are shown in Fig. 3. Periodic boundary conditions are applied on bulk and confined configurations in all three dimensions. The silica surface and water molecules are modeled using parameters from CLAYFF[46] and flexible SPC/E forcefields,[47] respectively. The OPLS/AA forcefield is used to model Ca^{2+} and CO_3^{2-} ions.[48] Table S1† summarizes the interatomic potentials.

The bulk and confined configurations are optimized through energy minimization using the "steepest descent" approach for 50 000 steps. NVT simulations are performed on the bulk and confined solutions for 50 ns. The temperature is held constant at 298 K using a Nose–Hoover thermostat with a relaxation time of 0.1 ps.[49,50] The intermolecular interactions of the simulated systems are calculated as the sum of the electrostatic contributions for all Coulomb interactions between the partial atomic charges and a short-range van der Waals dispersive interactions, given by the Lennard-Jones potential. The equation of motion is integrated using the leap-frog algorithm with a time step of 1 fs. The short-range interactions are calculated within a cutoff of 1.4 nm, while the long-range electrostatic interactions are treated using Particle Mesh Ewald (PME).[51] The non-bonded van der Waals and electrostatic interactions are modeled using 12-6 Lennard-Jones and coulombic models, respectively. The bonded interactions are accounted for in bond stretching, angles bending and dihedrals, except for silica matrix where only OH bond stretching is considered. All the simulations are conducted using GROningen Machine for Chemical Simulations (GROMACS 2018) simulation package.[52]

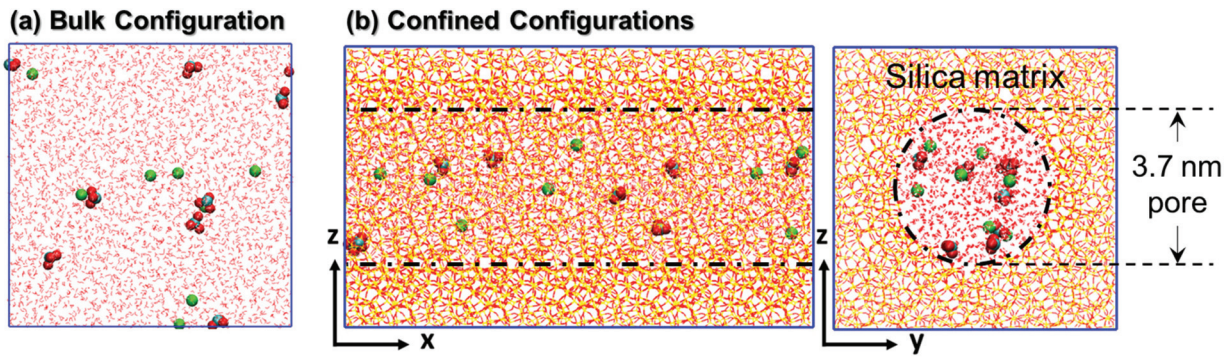

Fig. 3 Snapshots of the initial configurations of (a) bulk and (b) confined $CaCO_3$ solutions in cylindrical silica nanopores with diameter of 3.7 nm. Calcium and carbonate atoms are shown in VDW drawing method while water and silica atoms are shown in Lines drawing method implemented in VMD software.

3. Results and discussion

3.1. Synthesis of silica nanochannels (SNCs)

Sol–gel synthesis approaches provide unprecedented tunable controls on the particle and pore morphologies of architected siliceous materials.[53,54] The concept of dissolving a surfactant (*e.g.*, CTAB) and introducing and condensing silica around surfactant templates to direct sol–gel formation has opened opportunities to synthesize particle and pore morphologies with specific shapes and sizes. For example, amorphous silica,[53] forsterite (Mg_2SiO_4),[54] and wollastonite ($CaSiO_3$)[55] with ordered pores ranging from 2–20 nm can be architected based on advances in sol–gel and hydrothermal syntheses. One of the less explored approaches involves creating silica nanochannels in existing porous templates to develop predictive controls over carbon mineralization in confinement. Architecting these materials to study carbon mineralization pathways will unlock unprecedented controls into the mechanisms underlying carbonate formation in nanoconfined environments. To address this challenge, architected silica nanochannels are developed in alumina membranes (Fig. 2). The absence of any crystallinity in amorphous alumina membranes (AAMs) (by Cytiva Whatman™ Anodisc™ and procured from Fisher Scientific) is evident from the XRD patterns in Fig. S3(a).† These commercially available AAM materials have pore sizes of ~200 nm as evident from the SEM image in Figure. S3(b).†

The changes in the weight% of as-synthesized SNCs in AAMs before and after CTAB removal are determined using thermogravimetric analysis (TGA) are shown in Fig. S1(a).† For comparison, the TGA curve of as-received AAM is also shown. The major weight loss for as-prepared SNCs in AAMs is noted around 250 °C, corresponding to the removal of CTAB.[56–59] The SNCs formed inside the pores of AAMs are imaged by dissolving the amorphous alumina components in 10 wt% H_3PO_4 solution for 24 hours and recovering SNCs *via* centrifugation. The SEM image of SNCs obtained from dissolving the surrounding anodic alumina constituents is shown in Fig. 4(a). The formation of SNCs along the length of the membrane is noted in this image. The cylindrical orientation of SNCs is evident from the TEM image in Fig. 4(b). The outer diameter of the nanochannels formed inside the pores of AAMs is ~200 nm which is comparable to the pore size in AAMs. The uniformity and consistent lengths of the silica nanochannels throughout the membranes evident from the TEM and SEM images in Fig. 4 show the complete filling of AAM pores with the sol–gel precursor leading to the formation of morphologically and chemically uniform SNCs. The average pore size, pore volume, and specific surface area of SNCs in AAMs are 3.77 nm, 0.11 cc g^{-1}, and 57.17 m^2 g^{-1}, respectively. These parameters are determined using the NLDFT method with a cylindrical silica pores model at 77 K for liquid N_2. The uniformity of pore size distributions of SNCs with a pore diameter of 3.7 nm is evident in Fig. 4(c). The pore sizes and surface areas of AAM and SNCs in AAM are reported in Table 1.

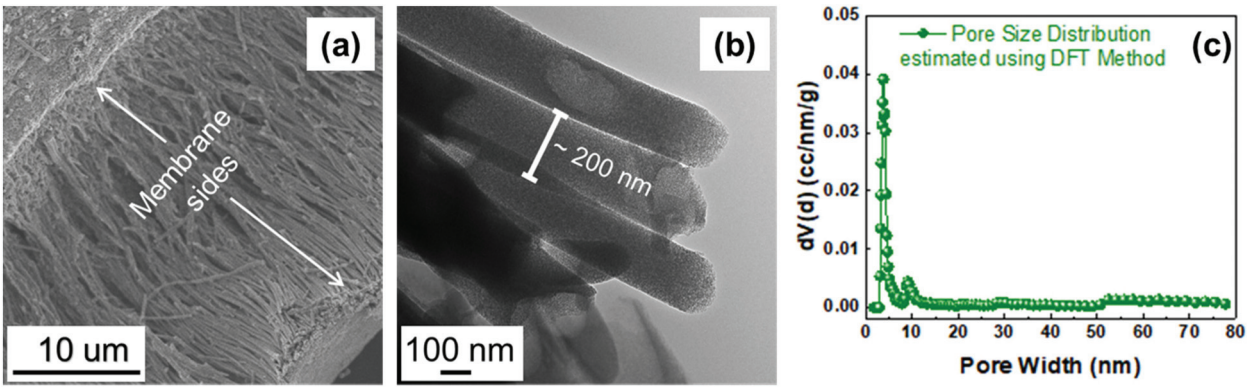

Fig. 4 (a) Silica nanochannels (SNCs) formed inside the alumina membrane as viewed using scanning electron microscopy (SEM) after dissolution of alumina membrane using 10 wt% H_3PO_4. (b) High resolution imaging of SNCs using transmission electron microscope (TEM). (c) The pore size distribution of SNCs determined using N_2 adsorption–desorption measurements.

Table 1 Estimated pore sizes, pore volumes, and surface areas for anodic alumina membrane (AAM) and AAM containing silica nanochannels (AAM-SNC). The values are obtained from N_2 adsorption–desorption measurements using multi-point BET and non-local density functional theory models. Surface area from multi-point BET is obtained by fitting the first 7 points on the adsorption isotherm. Pore volume for AAM can not be estimated using the NLDFT or BJH method for AAM materials

Sample ID	Pore size (nm)	Pore volume (cc g^{-1})	Surface area (m^2 g^{-1})
Anodic alumina membrane (AAM)	200 (SEM)	—	8.31 (multi-point BET)
Silica nanochannels (AAM-SNC)	3.7 (NLDFT)	0.11 (NLDFT)	71.65 (multi-point BET) 57.17 (NLDFT)

3.2 Formation of calcium carbonates in silica nanochannels (SNCs)

The hypothesis that nanoscale confinement contributes to the oriented growth of calcium carbonate is investigated by injecting a solution comprising a mixture of 0.1 M $Ca(NO_3)_2$ and 0.1 M $NaHCO_3$ solutions into silica nanochannels to grow calcium carbonate. The formation of calcium carbonate in silica nanochannels is evident from thermogravimetric analyses. The weight loss associated with the dissociation of calcium carbonate on heating is evident from Fig. S1(b).† Calcium carbonate formation is determined by collecting XRD data at 6, 18, and 30 hours after loading the calcium nitrate and sodium bicarbonate solutions into silica nanochannels. The XRD patterns (Fig. 5) reveal the dominant growth of the (104) plane of calcium carbonate followed by the (214) plane. In rhombohedral calcite, the typical dominant planes are (104), (113), (018), and (116). In contrast, the dominant planes in orthorhombic aragonite are (111), (021), (012), (112), and (221). In metastable vaterite with hexagonal crystal habitat, the dominant planes are (100), (101), (102), and (110). Complete XRD patterns of these polymorphs of calcium carbonate are shown in Fig. S4† for comparison. The prominent planes that distinguish calcite, aragonite, and vaterite phases are (104), (111), and (101), corresponding to the *d*-spacings of 3.03 Å, 3.39 Å, and 3.29 Å, respectively.[60,61] These results suggest that calcite, the most stable polymorph of calcium carbonate is the preferred phase for durable carbon storage. In this context, it is essential to consider differences in the stabilities of various polymorphs of calcium carbonate. Calcite is a stable anhydrous polymorph of $CaCO_3$ with very low solubility in water and remains unaltered over geological timescales. In contrast, aragonite is a metastable anhydrous $CaCO_3$, which is thermodynamically unstable at standard temperature and pressure conditions, and is converted to calcite in the presence of water due to its higher solubility in water.[62] Vaterite is another metastable anhydrous polymorph of $CaCO_3$ and does not exist under ambient conditions. Vaterite is transformed to aragonite or calcite upon interaction with water and is relatively rare in geological settings.[62,63] Atomistic simulations on the energetic stability of these polymorphs of $CaCO_3$ reveal that the (104) calcite surface is the most stable, having the lowest surface energy value of 0.51 J m^{-2}. In contrast, the carbonate terminated surface of aragonite has a smaller surface energy of 0.83 J m^{-2} for the (111) plane. The surface energy for the carbonate terminated (101) plane in vaterite is 0.79 J m^{-2}.[64] These results show that the energetically efficient polymorph of $CaCO_3$ is calcite.

In our XRD results, the distinct formation of (104) planes and the absence of (111) and (101) planes in this study are indicative of the formation of calcite in silica nanochannels (Fig. 5). The preferential growth of calcite along the (104) plane is attributed to the lowest density of surface broken bonds among the other calcite surfaces[65,66] and surface energy,[65,67,68] and an equal number of positive and negative charges.[69] Further, the (104) plane follows a flat (F) character as shown in Fig. 5(c).[70] The (214) plane becomes statistically significant after reaction for 30 hours. The reflections from the (214) plane can emerge from the particle growing in the vicinity of the nanochannel wall and appears to develop its characteristic "step-like" (S) nature as the growth along with the dominant (104) plane proceeds. The schematic comparison of flat (F) and "step-like" (S) profiles for (104) and (214) planes along [441] zone axis is shown in Fig. 5(c). The crystallite sizes of 1.3 nm, 1.8 nm, and 1.9 nm after 6 hours, 18 hours, and 30 hours, respectively, indicate a sluggish growth after first 6 hours (Fig. 5(b)). The growth of the calcite phases is slower between 18 hours and 30 hours likely due to pore size constraints.[65] These measurements show the preferential formation of stable calcite phases over metastable calcium carbonates in nanoscale confinement several hours after loading the initial solution bearing calcium and bicarbonate ions into the nanochannels.

The sizes of the calcium carbonate crystallites are estimated from the XRD data using the Scherrer equation (shown in eqn (i)).[71,72] In eqn (i), D represents the average crystallite size, K = 0.9 is Scherrer constant, λ is the wavelength of X-ray source used (Cu Kα = 0.154 nm), 2θ is Bragg angle, and $B(2\theta)$ is the

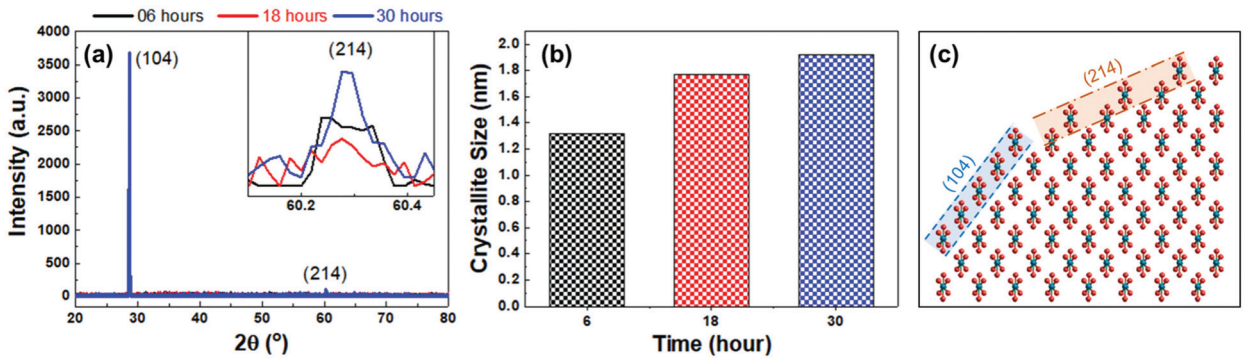

Fig. 5 (a) Identification of stable calcite phases inside silica nanochannels (SNCs) acquired at different time intervals using X-ray diffraction (XRD). (b) Crystallite sizes determined using Scherrer equation. (c) Schematic representation of calcite structure and growing (104) and (214) plane projected along the [441] zone axis.[70]

full width at half maximum (FWHM). The units of θ and $B(2\theta)$ are radians.

$$D = \frac{K \cdot \lambda}{B(2\theta) \cdot \cos\theta} \quad \text{(i)}$$

Based on this expression, the crystallite sizes of calcite are estimated to be 1.3 nm, 1.8 nm, and 1.9 nm after 6 hours, 18 hours, and 30 hours of reaction time, respectively (Fig. 5(b)). The growth of the calcite phases is slower between 18 hours and 30 hours likely due to spatial constraints of the pore size.[65] These measurements directly suggest the formation of stable calcite phases preferentially over metastable calcium carbonates in nanoscale confinement several hours after loading the initial solution bearing calcium and bicarbonate ions into the nanochannels. The preferential orientation planes of calcite are (104) and (214) planes (Fig. 5(a) and (c)).

Prior studies investigating the formation of calcium carbonate in confinement showed that in track etch (TE) – membrane polycarbonate with micrometer-sized pores[73] and fungal hyphae tubular cells, amorphous calcium carbonate (ACC) is formed initially.[74] The amorphous calcium carbonate eventually transforms into calcite and aragonite phases. In TE-membrane polycarbonate with pore diameters of 25 nm, 50–800 nm, and 1200 nm, aragonite, aragonite and calcite, and calcite are formed respectively at room temperature.[75] The formation of calcite in cylindrical pores of TE-membranes reported by Loste and co-workers[73] is consistent with the findings of this study. Moreover, pH has a significant impact on the formation of calcium carbonate polymorphs. For example, calcite-like ACC and vaterite-like ACC are obtained at pH ~ 8.75 and 9.8 or higher, respectively. Aragonite-like ACC is obtained in multi-component ionic environments including in the presence of Mg^{2+} ions.[76] The pH of the solution in the silica nanochannels is closer to 8.75, which aligns with the initial formation of calcite-like ACC structure before transforming into calcite. Fewer water molecules in the coordination environment of Ca^{2+} ions[77–79] in confinement compared to bulk fluids contribute to the formation of stable calcium carbonate. Fewer carbonate ions in the first coordination shell of

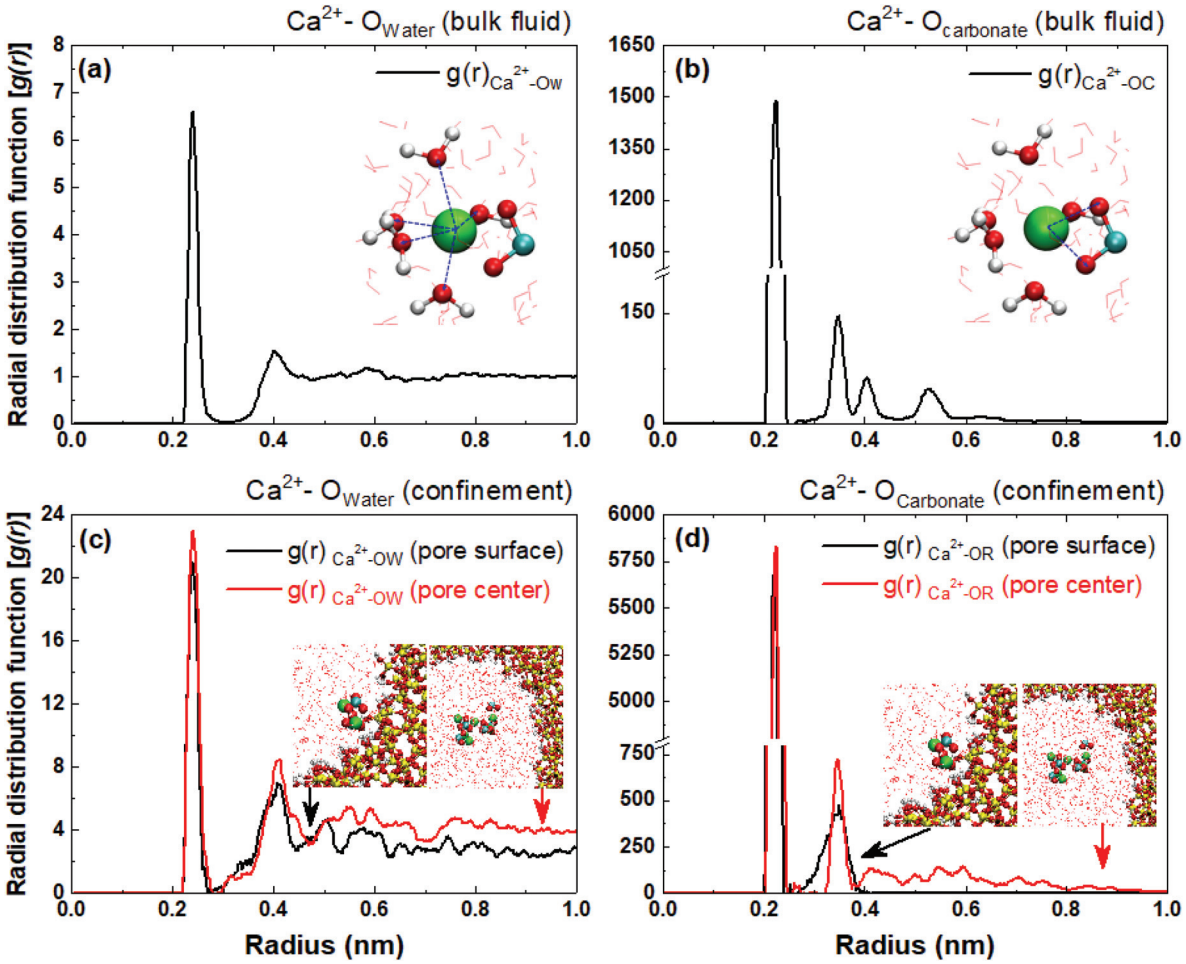

Fig. 6 Radial distribution function [$g(r)$] as a function of radius. (a) Calcium (Ca^{2+})–water oxygen (O_W) in bulk fluid. Inset: water in the first coordination shell of Ca^{2+} ion. (b) Ca^{2+}–Carbonate oxygen (O_R) in bulk fluid. Inset: carbonate in the first coordination shell of Ca^{2+} ion. (c) Ca^{2+}–O_W in confinement (silica nanochannel). (d) Ca^{2+}–O_R in confinement. Insets in (c & d): Ca^{2+} and CO_3^{2-} ions in the pore center and at pore surface.

Ca^{2+} ions favor stable calcite formation over metastable aragonite.[80] Additional factors to consider in the context of selective calcium carbonate polymorphs include confinement-induced ion transport, concentration profiles, and changes in the probability of nucleation.[28] The influence of ion transport, cation hydration behavior, and concentration profiles on the formation of specific calcium carbonate polymorphs are investigated using molecular dynamics simulations and discussed in the section below.

3.3 Influence of ion hydration and transport on calcium carbonate formation

Fundamental mechanistic insights into the organization, hydration, and transport of ions in confinement leading to calcium carbonate ($CaCO_3$) formation in silica nanopores are investigated using MD simulations. Simulations are performed in bulk and in confined fluids to contrast ion organization, hydration, and transport behavior leading to $CaCO_3$ formation in these environments. The static structure of the pre-nucleated $CaCO_3$ solutions in bulk and confined fluids is described by the radial distribution function ($g(r)$) (Fig. 6) and the corresponding coordination number ($n(r)$) (Fig. 7) of water-oxygen (O_{water}) and carbonate-oxygen ($O_{carbonate}$) atoms in the first coordination shell of Ca^{2+} ions. $g(r)$ and $n(r)$ are averaged over the last 10 ns of the simulation time to ensure equilibrated structure of water- and carbonate-oxygen in the first coordination shell of Ca^{2+} ions. The number of water molecules in the first coordination shell of Ca^{2+} ions in bulk environments is about 7.2, which is consistent with reported X-ray scattering measurements and molecular simulation studies.[81] It is interesting to note that a higher number of oxygen atoms corresponding to CO_3^{2-} ions are evident in the

Table 2 The number of water oxygen (O_{water}) and carbonate oxygens ($O_{carbonate}$) in the first coordination shell of Ca^{2+}. Error bars represent the standard deviation from the mean values of three different simulations

	Bulk fluid	Away from pore surface	At pore surface
O_{water}	$3.60 \pm 4 \times 10^{-2}$	$3.03 \pm 3 \times 10^{-2}$	$2.55 \pm 5 \times 10^{-2}$
$O_{carbonate}$	$4.23 \pm 3 \times 10^{-2}$	$4.51 \pm 1 \times 10^{-2}$	$4.08 \pm 3 \times 10^{-2}$

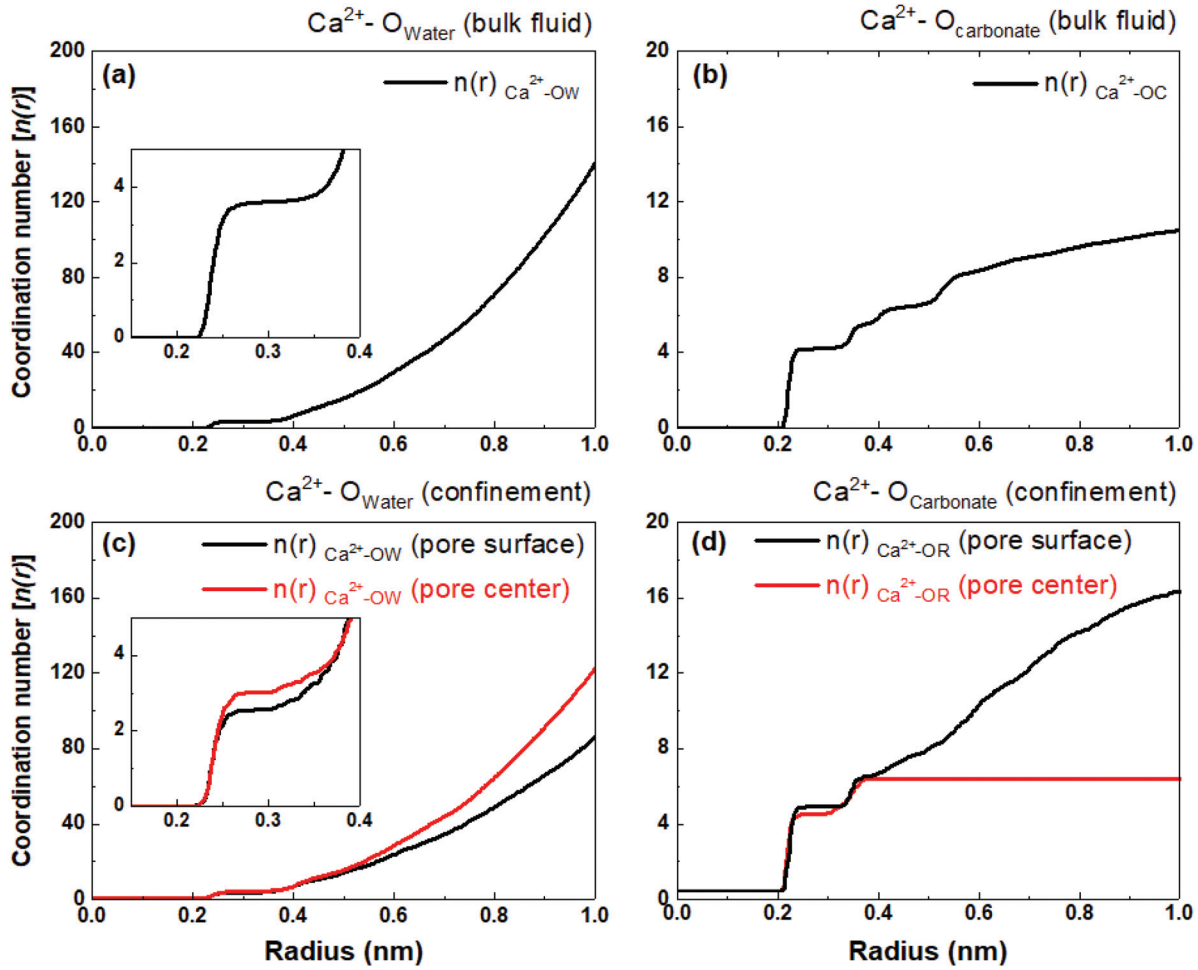

Fig. 7 Coordination number [$n(r)$] as a function of radius. (a) Calcium (Ca^{2+})–water oxygen (O_W) in bulk fluid. (b) Ca^{2+}–Carbonate oxygen (O_R) in bulk fluid. (c) Ca^{2+}–O_W in confinement (silica nanochannel). (d) Ca^{2+}–O_R in confinement.

Table 3 The self-diffusion coefficient (10^{-5} cm^2 s^{-1}) of Ca^{2+}, CO_3^{2-} and water in bulk and in confined systems. Error bars represent the standard deviation from the mean values of three different simulations

		Confinement	
	Bulk fluid	Away from pore surface	At pore surface
Ca^{2+}	$63.0 \times 10^{-2} \pm 3 \times 10^{-2}$	$10.6 \times 10^{-2} \pm 4 \times 10^{-3}$	$0.24 \times 10^{-3} \pm 4 \times 10^{-5}$
CO_3^{2-}	$62.8 \times 10^{-2} \pm 2 \times 10^{-2}$	$13.8 \times 10^{-2} \pm 6 \times 10^{-3}$	$4.92 \times 10^{-3} \pm 2 \times 10^{-4}$
Water	$251.0 \times 10^{-2} \pm 12 \times 10^{-2}$	$67.7 \times 10^{-2} \pm 9 \times 10^{-3}$	$21.10 \times 10^{-3} \pm 8 \times 10^{-4}$

first coordination shell of Ca^{2+} ions compared to oxygen atoms corresponding to water molecules (Fig. 7(a) and Table 2). The number of oxygen atoms corresponding to the carbonate ions in the first coordination shell of Ca^{2+} cations is 4.23 ± 0.03 (Fig. 7(b) and Table 2), which is in agreement with the findings of Wang and co-workers after accounting for the difference in the solutions' concentrations.[82] Confinement induces significant changes in the hydration structure of Ca^{2+} ions such that it reduces the number of oxygen atoms corresponding to the water molecules in the first coordination shell of the Ca^{2+} ion compared to the bulk fluids. The number of oxygen atoms corresponding to the water molecules in the nanopores decreased to $3.03 \pm 3 \times 10^{-2}$ and $2.55 \pm 5 \times 10^{-2}$ in the first coordination shells of the Ca^{2+} ion in the pore center and at the pore surface, respectively (see Table 2). The dehydration of Ca^{2+} ions in the nanopores is associated with the structural alterations of oxygen atoms corresponding to the carbonate species in the first coordination shell of the Ca^{2+} ion. The number of oxygen atoms corresponding to the carbonate species in the first coordination shell increases to $4.51 \pm 1 \times 10^{-2}$ for the Ca^{2+} ion in the pore center while it decreases to $4.08 \pm 3 \times 10^{-2}$ for Ca^{2+} ions at the pore surface (see Table 2). The dehydration of calcium carbonates, mainly by heating, promotes the transformation of amorphous to crystalline morphologies such as the transformation of amorphous calcium carbonate (ACC) to mesostructured calcite.[77–79] Thus, fewer water molecules in the coordination environment of Ca^{2+} ions in confined fluids provide another dehydration pathway to tune the transformation of metastable amorphous carbonate structures to crystalline calcite morphologies.

Confinement is also found to have a significant influence on the transport behavior of ions. Significant differences are noted in the self-diffusion coefficients and the local distribution of Ca^{2+}, CO_3^{2-} and water in bulk fluids and those confined in pores. In bulk fluids, the diffusion coefficients of Ca^{2+}, CO_3^{2-} and water molecules are $(0.63 \pm 0.03) \times 10^{-5}$, $(0.63 \pm 0.02) \times 10^{-5}$ and $(2.51 \pm 0.12) \times 10^{-5}$ cm^2 s^{-1}, respectively (Table 3). These values are consistent with the diffusion coefficients reported by Wang and co-workers.[82]

Significant differences in the diffusion coefficients of ions in bulk and confined fluids are noted. The diffusivity of Ca^{2+} and CO_3^{2-} ions at the pore surface is more than two orders of magnitude lower compared in the center of the pore due to surface diffusion. The nucleation and growth of calcium carbonate crystals are directly related to the diffusion of calcium and carbonate ions. Prior MD simulations and experiments showed that the nucleation rate of $CaCO_3$ crystals in bulk solvents increases exponentially with the enhanced diffusion of ions.[83] The diffusion of Ca^{2+} and CO_3^{2-} ions have been controlled by using various additives including other ions such as Na^+, Cl^- and OH^-,[84] glycerol,[83] and poly(acrylic acid) (PAA).[85] Reduced diffusivity of Ca^{2+} and CO_3^{2-} ions observed on adding these additives to the aqueous solutions is attributed to the formation of ion pairs between Ca^{2+} and CO_3^{2-} with the added ions, enhanced solution viscosity on adding glycerol and controlled the directional diffusion of ions in hydrogels using PAA. Furthermore, the morphology of the formed carbonate crystals can be tuned by controlling ion diffusion. In addition to the nucleation enhancement, slowing the diffusion of ions enables tuning the morphology of the formed carbonate crystals. In this context, Wang and co-workers[86] showed that a decrease in the diffusion of calcium and carbonate ions promotes the formation of vaterite and aragonite crystals and the joint effect of the diffusion-reaction leads to the formation of cubic and needle-like particles. Similarly, Jo and co-workers[87] found that the gradual decrease in the diffusion of ions results in morphological transitions from hopper-like to rosette-like and otoconia-like calcite structures. Kim and co-workers demonstrated that controlling the diffusion of the ions by adding poly(acrylic acid) in hydrogel results in a variety of calcite morphologies including elliptical and spherical calcite structures.[85] These studies support our finding that significantly reduced diffusivities of ions at the pore surface contributes to the formation of stable calcite phases.

4. Conclusions

Understanding the pathways of carbon mineralization in subsurface-related, silica-rich reservoirs is essential to meet the future goals of energy landscape. In this context, the mineralization mechanisms in reservoirs with nanoscale confinements needs investigation due to their abundance at the proposed mineralization sites. In this work, we study the nucleation of calcium carbonate in silica nanochannels having diameter = 3.7 nm and report the preferential formation of stable calcite phase over metastable aragonite or vaterite phases. From molecular dynamics simulations, we note relatively fewer water molecules of hydration and a higher number of carbonate ions surrounding calcium ion (Ca^{2+}) in confinement compared to bulk fluid. The number of oxygen atoms around Ca^{2+} in confinement is 6, which is a suitable condition for calcite for-

mation compared to aragonite formation (9 oxygen atoms). The formation of stable carbonates is favorable for the permanent storage of CO_2, especially in silica-rich reservoirs.

Conflicts of interest

There are no conflicts to declare.

Acknowledgements

The authors gratefully acknowledge the support of the College of Engineering at Cornell University and the NSF CAREER award (# 2144373). Electron microscopy imaging is made possible through the Cornell Center for Materials Research (CCMR) #DMR-1719875 supported by the National Science Foundation Materials Research Science and Engineering Centers (MRSEC) program (DMR 1120296).

Notes and references

1 J. F. B. Mitchell, *Rev. Geophys.*, 1989, **27**, 115–139.
2 J. S. Sawyer, *Nature*, 1972, **239**, 23–26.
3 A. D. McGuire, L. G. Anderson, T. R. Christensen, S. Dallimore, L. Guo, D. J. Hayes, M. Heimann, T. D. Lorenson, R. W. Macdonald and N. Roulet, *Ecol. Monogr.*, 2009, **79**, 523–555.
4 S. J. Davis, N. S. Lewis, M. Shaner, S. Aggarwal, D. Arent, I. L. Azevedo, S. M. Benson, T. Bradley, J. Brouwer, Y.-M. Chiang, C. T. M. Clack, A. Cohen, S. Doig, J. Edmonds, P. Fennell, C. B. Field, B. Hannegan, B. Hodge, M. I. Hoffert, E. Ingersoll, P. Jaramillo, K. S. Lackner, K. J. Mach, M. Mastrandrea, J. Ogden, P. F. Peterson, D. L. Sanchez, D. Sperling, J. Stagner, J. E. Trancik, C. Yang and K. Caldeira, *Science*, 2018, **360**, 1–9.
5 R. S. Haszeldine, S. Flude, J. Gareth and V. Scott, *Philos. Trans. R. Soc., A*, 2018, **376**, 1–23.
6 P. J. A. Kenis, A. Dibenedetto and T. Zhang, *ChemPhysChem*, 2017, **18**, 3091–3093.
7 Z. Zhang, S. Pan, H. Li, J. Cai, A. Ghani, E. John and V. Manovic, *Renewable Sustainable Energy Rev.*, 2020, **125**, 109799.
8 G. Gadikota, *Nat. Rev. Chem.*, 2020, **4**, 78–89.
9 B. Sigf, C. Marieni, D. G. Sigur and E. H. Oelkers, *Nat. Rev. Earth Environ.*, 2020, **1**, 90–102.
10 B. P. Mcgrail, F. A. Spane, E. C. Sullivan, D. H. Bacon and G. Hund, *Energy Procedia*, 2011, **4**, 5653–5660.
11 G. Gadikota, A. hyung and A. Park, *Accelerated Carbonation of Ca- and Mg-Bearing Minerals and Industrial Wastes Using CO2*, Elsevier B.V., 2015.
12 E. Environ, A. Sanna, R. Hall and M. Maroto-valer, *Energy Environ. Sci.*, 2012, **5**, 7781–7796.
13 J. M. Matter, W. S. Broecker, M. Stute, S. R. Gislason, E. H. Oelkers, A. Stefánsson, D. Wolff-Boenisch, E. Gunnlaugsson, G. Axelsson and G. Björnsson, *Energy Procedia*, 2009, **1**, 3641–3646.
14 P. B. Kelemen and J. Matter, *Proc. Natl. Acad. Sci. U. S. A.*, 2008, **105**, 17295–17300.
15 Q. R. S. Miller, D. A. Dixon, S. D. Burton, E. D. Walter, D. W. Hoyt, A. S. Mcneill, J. D. Moon, K. S. Thanthiriwatte, E. S. Ilton, O. Qafoku, C. J. Thompson, H. T. Schaef, K. M. Rosso and J. S. Loring, *J. Phys. Chem. C*, 2019, **123**, 12871–12885.
16 Q. R. S. Miller, M. E. Bowden, J. P. Kaszuba and H. T. Schaef, *Chem. Commun.*, 2019, **55**, 6835–6837.
17 I. Rigopoulos, K. C. Petallidou, M. A. Vasiliades, A. Delimitis, I. Ioannou, A. M. Efstathiou and T. Kyratsi, *Powder Technol.*, 2015, **273**, 220–229.
18 M. Hänchen, V. Prigiobbe, R. Baciocchi and M. Mazzotti, *Chem. Eng. Sci.*, 2008, **63**, 1012–1028.
19 J. A. Kittrick and F. J. Peryea, *Soil Sci. Soc. Am. J.*, 1986, **50**, 243–247.
20 C. Rodríguez-Navarro, E. Ruiz-Agudo, J. Harris and S. E. Wolf, *J. Struct. Biol.*, 2016, **196**, 260–287.
21 S. Gopi, V. K. Subramanian and K. Palanisamy, *Mater. Res. Bull.*, 2013, **48**, 1906–1912.
22 J. K. Moore, J. A. Surface, A. Brenner, P. Skemer, M. S. Conradi and S. E. Hayes, *Environ. Sci. Technol.*, 2015, **49**, 657–664.
23 D. W. Ming and T. William, *Soil Sci. Soc. Am. J.*, 1985, **49**, 1303–1308.
24 C. M. Janet, B. Viswanathan, R. P. Viswanath and T. K. Varadarajan, *J. Phys. Chem. C*, 2007, **111**, 10267–10272.
25 A. M. Belcher, X. H. Wu, R. J. Christensen, P. K. Hansma, G. D. Stucky and D. E. Morsetll, *Nature*, 1996, **381**, 56–58.
26 F. C. Meldrum and H. Co, *Chem. Rev.*, 2008, **108**, 4332–4432.
27 S. Mann, D. D. Archibald, J. M. Didymus, T. Douglas, B. R. Heywood, F. C. Meldrum and N. J. Reeves, *Science*, 1993, **261**, 1286–1292.
28 Y. Wang, M. Zeng, F. C. Meldrum and H. K. Christenson, *Cryst. Growth Des.*, 2017, **17**, 6787–6792.
29 J. W. Mullin, *Crystallization*, Butterworth-Heinemann, Oxford, 3rd edn, 1993.
30 W. K. Burton, N. Cabrera and F. C. Frank, *Philos. Trans. R. Soc., A*, 1951, **243**, 299–358.
31 J. J. De Yoreo, L. A. Zepeda-Ruiz, R. W. Friddle, S. R. Qiu, L. E. Wasylenki, A. A. Chernov, G. H. Gilmer and P. M. Dove, *Cryst. Growth Des.*, 2009, **9**, 5135–5144.
32 W. Ostwald, *Z. Phys. Chem.*, 1897, **22**, 289–330.
33 C. Y. Tai and F. B. Chen, *AIChE J.*, 1998, **44**, 1790–1798.
34 A. Navrotsky, *Proc. Natl. Acad. Sci. U. S. A.*, 2004, **101**, 12096–12101.
35 Y. U. T. Gong, C. E. Killian, I. C. Olson, N. P. Appathurai, A. L. Amasino, M. C. Martin, L. J. Holt, F. H. Wilt and P. U. P. A. Gilbert, *Proc. Natl. Acad. Sci. U. S. A.*, 2012, **109**, 6088–6093.
36 M. Schiro, E. Ruiz-Agudo and C. Rodríguez-Navarro, *Phys. Rev. Lett.*, 2012, **26**, 265503, 190AD.

37 R. L. Penn and J. F. Banfield, *Science*, 1998, **281**, 969–971.
38 R. L. Penn and J. A. Soltis, *CrystEngComm*, 2014, **16**, 1409–1418.
39 R. Sathiyanarayanan, M. Alimohammadi, Y. Zhou and K. A. Fichthorn, *J. Phys. Chem. C*, 2011, **115**, 18983–18990.
40 G. Gadikota and A. H. A. Park, *Accelerated Carbonation of Ca- and Mg-Bearing Minerals and Industrial Wastes Using CO2*, 2014.
41 S. Zhang, Z. Zhang, Y. Lu, M. Rostam-Abadi and A. Jones, *Bioresour. Technol.*, 2011, **102**, 10194–10201.
42 T. N. Patel, A. H. A. Park and S. Banta, *Biotechnol. Bioeng.*, 2013, **110**, 1865–1873.
43 L. Ji, L. Zhang, X. Zheng, L. Feng, Q. He, Y. Wei and S. Yan, *J. CO2 Util.*, 2021, **51**, 101653.
44 B. Yu, H. Yu, K. Li, L. Ji, Q. Yang, X. Wang, Z. Chen and M. Megharaj, *Environ. Sci. Technol.*, 2018, **52**, 13629–13637.
45 M. Liu, A. Hohenshil and G. Gadikota, *Energy Fuels*, 2021, **35**, 8051–8068.
46 R. T. Cygan, J. J. Liang and A. G. Kalinichev, *J. Phys. Chem. B*, 2004, **108**, 1255–1266.
47 H. J. C. Berendsen, J. R. Grigera and T. P. Straatsma, *J. Phys. Chem.*, 1987, **91**, 6269–6271.
48 W. L. Jorgensen, D. S. Maxwell and J. Tirado-Rives, *J. Am. Chem. Soc.*, 1996, **118**, 11225–11236.
49 S. Nosé, *Mol. Phys.*, 1984, **52**, 255–268.
50 W. G. Hoover, *Phys. Rev. A*, 1985, **31**, 1695–1697.
51 T. Darden, D. York and L. Pedersen, *J. Chem. Phys.*, 1993, **98**, 10089–10092.
52 M. J. Abraham, T. Murtola, R. Schulz, S. Páll, J. C. Smith, B. Hess and E. Lindah, *SoftwareX*, 2015, **1–2**, 19–25.
53 S.-H. Wu, C.-Y. Mou and H.-P. Lin, *Chem. Soc. Rev.*, 2013, **42**, 3862–3875.
54 X. Gao, H. Asgar, I. Kuzmenko and G. Gadikota, *Microporous Mesoporous Mater.*, 2021, **327**, 111381.
55 J. Wei, F. Chen, J. Shin, H. Hong, C. Dai, J. Su and C. Liu, *Biomaterials*, 2009, **30**, 1080–1088.
56 S. A. Araujo, M. Ionashiro, V. J. Fernandes Jr. and A. S. Araujo, *J. Therm. Anal. Calorim.*, 2001, **64**, 801–805.
57 R. Denoyel, M. T. J. Keene, P. L. Lllewellyn and J. Rouquerol, *J. Therm. Anal. Calorim.*, 1999, **56**, 261–266.
58 J. Goworek, A. Kierys, W. Gac, A. Borówka and R. Kusak, *J. Therm. Anal. Calorim.*, 2009, **96**, 375–382.
59 M. J. B. Souza, A. O. S. Silva, J. M. F. B. Aquino, V. J. Fernandes Jr. and A. S. Araújo, *J. Therm. Anal. Calorim.*, 2004, **75**, 693–698.
60 C. G. Kontoyannis and N. V. Vagenas, *Analyst*, 2000, **125**, 251–255.
61 J. Chen and L. Xiang, *Powder Technol.*, 2009, **189**, 64–69.
62 M. M. H. Al Omari, I. S. Rashid, N. A. Qinna, A. M. Jaber and A. A. Badwan, in *Profiles of Drug Substances, Excipients and Related Methodology*, ed. H. G. Brittain, Academic Press, 2016, vol. 41, pp. 31–132.
63 J. Wang and U. Becker, *Am. Mineral.*, 2009, **94**, 380–386.
64 W. Sekkal and A. Zaoui, *Sci. Rep.*, 2013, **3**, 1–10.
65 Z. Gao, C. Li, W. Sun and Y. Hu, *Colloids Surf., A*, 2017, **520**, 53–61.
66 G. A. O. Zhi-yong, S. U. N. Wei, H. U. Yue-hua and L. I. U. Xiao-wen, *Trans. Nonferrous Met. Soc. China*, 2012, **22**, 1203–1208.
67 M. F. Roberto, B. Marco and A. Dino, *Cryst. Growth Des.*, 2010, **10**, 4096–4100.
68 M. Bruno, F. R. Massaro, M. Rubbo, M. Prencipe and D. Aquilano, *Cryst. Growth Des.*, 2010, **10**, 3102–3109.
69 D. Aquilano, F. Otálora, L. Pastero and J. M. García-ruiz, *Prog. Cryst. Growth Charact. Mater.*, 2016, **62**, 227–251.
70 D. Aquilano, M. Bruno, F. R. Massaro, M. Rubbo, V. V. Caluso and I. Torino, *Cryst. Growth Des.*, 2011, **11**, 3985–3993.
71 X. Gao, H. Asgar, I. Kuzmenko and G. Gadikota, *Microporous Mesoporous Mater.*, 2021, **327**, 111381.
72 H. P. Klug and L. E. Alexander, *X-ray Diffraction Procedures for Polycrystalline and Amorphous Materials*, Wiley, New York, 2nd edn, 1974.
73 E. Loste, R. J. Park, J. Warren and F. C. Meldrum, *Adv. Funct. Mater.*, 2004, **14**, 1211–1220.
74 A. Livne, S. C. Mijowska, I. Polishchuk, W. Mashikoane, A. Katsman and B. Pokroy, *J. Mater. Chem. B*, 2019, **7**, 5725–5731.
75 M. Zeng, Y. Y. Kim, C. Anduix-Canto, C. Frontera, D. Laundy, N. Kapur, H. K. Christenson and F. C. Meldrum, *Proc. Natl. Acad. Sci. U. S. A.*, 2018, **115**, 7670–7675.
76 A. Fernandez-Martinez, B. Kalkan, S. M. Clark and G. A. Waychunas, *Angew. Chem.*, 2013, **125**, 8512–8515.
77 C. Rodriguez-Navarro, K. Kudlacz, O. Cizer and E. Ruiz-Agudo, *Cryst. Res. Technol.*, 2015, **17**, 58–72.
78 J. D. Rodriguez-Blanco, S. Shaw and L. G. Benning, *Nanoscale*, 2011, **3**, 265–271.
79 A. V. Radha, T. Z. Forbes, C. E. Killian, P. U. P. A. Gilbert and A. Navrotsky, *Proc. Natl. Acad. Sci. U. S. A.*, 2010, **107**, 16438–16443.
80 M. Saharay, A. O. Yazaydin and R. J. Kirkpatrick, *J. Phys. Chem. B*, 2013, **117**, 3328–3336.
81 D. Jiao, C. King, A. Grossfield, T. A. Darden and P. Ren, *J. Phys. Chem. B*, 2006, **110**, 18553–18559.
82 X. Wang, Y. Han, L. Lin, M. Fuji, T. Endo, H. Watanabe and M. Takahashi, *Model. Simul. Mater. Sci. Eng.*, 2008, **16**(3), 035006.
83 X. Dou, H. Huang and Y. Han, *Chin. J. Chem. Eng*.
84 B. Johannesson, K. Yamada, L. O. Nilsson and Y. Hosokawa, *Mater. Struct.*, 2007, **40**(7), 651–665.
85 H. L. Kim, Y. S. Shin and S. H. Yang, *CrystEngComm*, 2022, 42–44.
86 H. Wang, W. Huang and Y. Han, *Particuology*, 2013, **11**, 301–308.
87 M. K. Jo, Y. Oh, H. J. Kim, H. L. Kim and S. H. Yang, *Cryst. Growth Des.*, 2020, **20**, 560–567.